The Astrophysical Journal, 606:625–634, 2004 May 10

STRUCTURE OF DARK MATTER HALOS FROM HIERARCHICAL CLUSTERING. III. SHALLOWING OF THE INNER CUSP

Toshiyuki Fukushige
Department of General Systems Studies, College of Arts and Sciences, University of Tokyo, 3-8-1 Komaba, Meguro-ku, Tokyo 153, Japan

Atsushi Kawai
Faculty of Human and Social Studies, Saitama Institue of Technology, 1690 Fusaiji, Okabe, Ohsato, Saitama 369-0293, Japan

and

Junichiro Makino
Department of Astronomy, School of Sciences, University of Tokyo, 7-3-1 Hongo, Bunkyo-ku, Tokyo 117, Japan
Received 2003 June 10; accepted 2004 January 24

ABSTRACT

We investigate the structure of the dark matter halo formed in the cold dark matter scenarios by *N*-body simulations with a parallel tree code on GRAPE cluster systems. We simulated eight halos with the mass of 4.4×10^{14} to $1.6 \times 10^{15}\ M_\odot$ in SCDM and LCDM models using up to 30 million particles. With the resolution of our simulations, the density profile is reliable down to 0.2% of the virial radius. Our results show that the slope of inner cusp within 1% virial radius is shallower than -1.5, and the radius where the shallowing starts exhibits run-to-run variation, which means that the innermost profile is not universal.

Subject headings: cosmology: theory — dark matter — galaxies: clusters: general — methods: *N*-body simulations — galaxies: halos

On-line material: color figures

1. INTRODUCTION

Since the "finding" of the universal profile by Navarro, Frenk, & White (1996, 1997, hereafter NFW), the structure of dark matter halos formed through dissipationless hierarchical clustering from cosmological initial setting has been explored by many researchers. NFW performed a number of *N*-body simulations of the halo formation using 10–20 thousand particles and found that the profile of dark matter halo could be fitted to a simple formula (hereafter the "NFW profile"):

$$\rho = \frac{\rho_0}{(r/r_0)(1 + r/r_0)^2}, \tag{1}$$

where ρ_0 is a characteristic density and r_0 is a scale radius. They also argued that the profile has the same shape, independent of the halo mass, the power spectrum of the initial density fluctuation, or other cosmological parameters.

Several groups reported the results of similar simulations with much higher resolutions. However, disagreement concerning the inner structure still remains. Some researchers claimed that the slope of the inner cusp is steeper than that in the NFW's results. Fukushige & Makino (1997) performed a similar simulation with 768 k particles and found that a galaxy-sized halo has a cusp steeper than $\rho \propto r^{-1}$. Moore et al. (1998, 1999, hereafter M99) and Ghigna et al. (2000) performed simulations with up to 4 million particles and obtained the result that the profile has a cusp proportional to $r^{-1.5}$ in both galaxy-sized and cluster-sized halos. M99 proposed the modified universal profile (hereafter "M99 profile"),

$$\rho = \frac{\rho_0}{(r/r_0)^{1.5}[1 + (r/r_0)^{1.5}]}. \tag{2}$$

Fukushige & Makino (2001, 2003 [hereafter Papers I and II]) performed two series of *N*-body simulations and found that the halos have density cusps proportional to $r^{-1.5}$, independent of the halo mass and cosmological models.

On the other hand, other researchers obtained the slope of inner cusp shallower than -1.5 and close to that in the NFW profile. Jing & Suto (2000, 2002) performed a series of *N*-body simulations and concluded that the power of the cusp depends on mass. It varies from -1.5 for a galaxy mass halo to -1.1 for a cluster mass halo. Klypin et al. (2001) obtained a slope at the center that could be approximated by $r^{-1.5}$. They, however, argued that the NFW fit is still good up to their resolution limit. Power et al. (2003) simulated an LCDM galaxy-sized halo with 3 M particles and claimed that the circular velocity profile obtained is in better agreement with the NFW profile than with the M99 profile.

The purpose of this paper is to explore the inner structure of the dark matter halo by means of *N*-body simulations with about 10 times higher mass resolution than that of previous simulations. We simulated the formation of eight cluster-sized halos in the SCDM and LCDM models using a parallel Barnes-Hut tree code (Barnes & Hut 1986) on parallel GRAPE cluster.

The structure of this paper is as follows. In § 2 we describe the model of our *N*-body simulation. In § 3 we present the results of simulation. Section 4 is for oour conclusion and discussion.

2. SIMULATION METHOD

We consider two cosmological models, a SCDM model ($\Omega_0 = 1.0$, $h = 0.5$, $\sigma_8 = 0.6$) and a LCDM model ($\Omega_0 = 0.3$, $\lambda_0 = 0.7$, $h = 0.7$, $\sigma_8 = 1.0$). Here Ω_0 is the density parameter, λ_0 is the dimensionless cosmological constant, and $H_0 = 100\ h$ km s^{-1} Mpc^{-1} at the present epoch. The amplitudes of the power spectrum in CDM models are normalized using the top-hat filtered mass variance at 8 h^{-1} Mpc according to the cluster abundance (Kitayama & Suto 1997).

TABLE 1
RUN PROPERTIES

Model	Run	M_v ($M_\odot$)	r_v (Mpc)	N_v ($\times 10^6$)	N ($\times 10^6$)	m ($10^7 \times M_\odot$)	$1+z_i$
SCDM.....	S1	1.58×10^{15}	3.08	29.2	60.3	5.39	44.2
	S2	1.21×10^{15}	2.84	31.2	60.7	3.86	45.5
	S3	1.21×10^{15}	2.84	4.5	10.0	26.5	37.9
	S4	4.47×10^{14}	2.03	6.9	13.9	6.46	43.4
LCDM.....	L1	9.61×10^{14}	2.43	25.2	62.8	3.80	51.1
	L2	6.96×10^{14}	2.20	26.0	59.9	2.67	52.7
	L3	6.49×10^{14}	2.15	7.2	16.7	9.01	47.5
	L4	4.45×10^{14}	1.88	7.8	13.5	5.67	49.4

We simulate the formation of the dark matter halos using the "resimulation" method, which has been a standard method for the simulation of halo formation since NFW (1996). The procedure for setting the initial condition of halos is the same as that used in Paper II.

We first performed large-scale cosmological simulations with 3.7×10^6 particles in a sphere of 150 Mpc comoving radius. We regard spherical overdensity regions around local potential minima within r_v as candidate halos. We define the radius r_v such that the spherical overdensity inside is $178\Omega_0^{0.3}$ times the critical density for SCDM and $178\Omega_0^{0.4}$ times for LCDM model (Eke, Cole, & Frenk 1996).

We selected eight halos from the catalog of candidate halos. The selected halos are summarized in Table 1. We selected the three most massive halos and one halo randomly from halo candidates lying within 100 Mpc from the center in both models (so that the external tidal field can be included). We express a region within $5r_v$ from the center of the halo at $z = 0$ in the cosmological simulation with larger number of particles. We place particles whose mass is as same as that in the cosmological simulation in a sphere of $\sim$50 Mpc comoving radius surrounding the high-resolution region, in order to express the external tidal field. The total number of particles, N, is listed in Table 1. The generation of initial density fluctuation was done on the HITACHI SR8000 (1 node) at the Information Technology Center, University of Tokyo using the GRAPHIC2 package (Bertschinger 2001).

We integrate the system directly in the physical coordinates for both the cosmological and halo simulations. We used a leap-frog integrator with shared and constant time steps. The step size for the cosmological simulation is $\Delta t/(t_{\rm H} - t_i) = 1/1024$, and that for the halo simulation is 1/4096. Here $t_{\rm H}$ is the Hubble time and t_i is the time at which the simulation starts. The (Plummer) gravitational softening is constant in the physical coordinates and the length $\varepsilon_{\rm grav}$ is 5 kpc for the cosmological simulation, 1 kpc for runs S1, S2, L1, and L2, and 2 kpc for other runs of halo simulations.

The force calculation is done with the parallel Barnes-Hut tree code on GRAPE clusters (Kawai, Makino 2003).[1] GRAPE is a special-purpose computer designed to accelerate N-body simulations. The parallelization scheme that we used is basically the same as Warren & Salmon's (1993) Hashed Oct-Tree algorithm, except that we incorporated Barnes's (1990) modified algorithm. The modification is necessary in order to make GRAPE work efficiently (Makino 1991). We use only the dipole expansion and the opening parameter $\theta = 0.4$ for the cosmological simulation and $\theta = 0.5$ for the halo simulation.

For high-resolution halo simulations, we used both a parallel GRAPE-5 cluster at the University of Tokyo and a parallel MDGRAPE-2 cluster at RIKEN. The parallel GRAPE-5 cluster consists of eight host computers (Pentium 4/1.9 GHz, i845), each of which has one GRAPE-5 (Kawai et al. 2000) board. The parallel MDGRAPE-2 cluster consists of eight host computers (Pentium 4/2.2 GHz, i850), each of which has one MDGRAPE-2 (Susukita et al. 2003) board. For cosmological simulations we used one board GRAPE-5. The simulation presented below needs, for example in run S2, $\sim$300 s per time step, and thus one run (4096 time steps) is completed in 350 hr (wall-clock time) with the GRAPE-5 cluster.

3. RESULTS

3.1. *Snapshots*

Figures 1 and 2 show the particle distribution for run S2 at $z = 0.58$ and 0. The length of the side for each panel is 6.67 Mpc. For these plots, we shifted the origin of coordinates to the position of the potential minimum. In Table 1 we summarized the radius r_v, the mass M_v, and the number of particles N_v within r_v at $z = 0$.

3.2. *Density Profile*

Figures 3 and 4 show the density profiles of all runs at $z = 0$ for the SCDM and LCDM models, respectively. The exception is run L4, for which we plot the density profile at $z = 0.06$ because the merging process occurs just near the center of halos at $z = 0$. The position of the center of the halo was determined using the potential minimum, and the density was averaged over each spherical shell whose width is $\log_{10}(\Delta r) = 0.0172$. For illustrative purposes, the densities are shifted vertically.

We plot the densities by the thick lines only if the criteria for two-body relaxation introduced in Paper I, $t_{\rm rel}(r)/t > 3$, is satisfied, where $t_{\rm rel}(r)$ is the local two-body relaxation time given by

$$t_{\rm rel} = \frac{0.065v^3}{G^2 \rho m \ln (R_{\rm max}/\varepsilon)}, \tag{3}$$

(cf. Spitzer 1987) and $R_{\rm max}$ is a maximum impact parameter. Here we set $R_{\rm max}$ to 1 Mpc as a system size. We also confirmed that other numerical artifacts due to the time integration did not influence the density profile, as will be discussed in § 3.3.2. The potential softening does not influence the profile, as will be discussed in § 3.3.3.

[1] The source code for both serial and parallel implementations are available upon request.

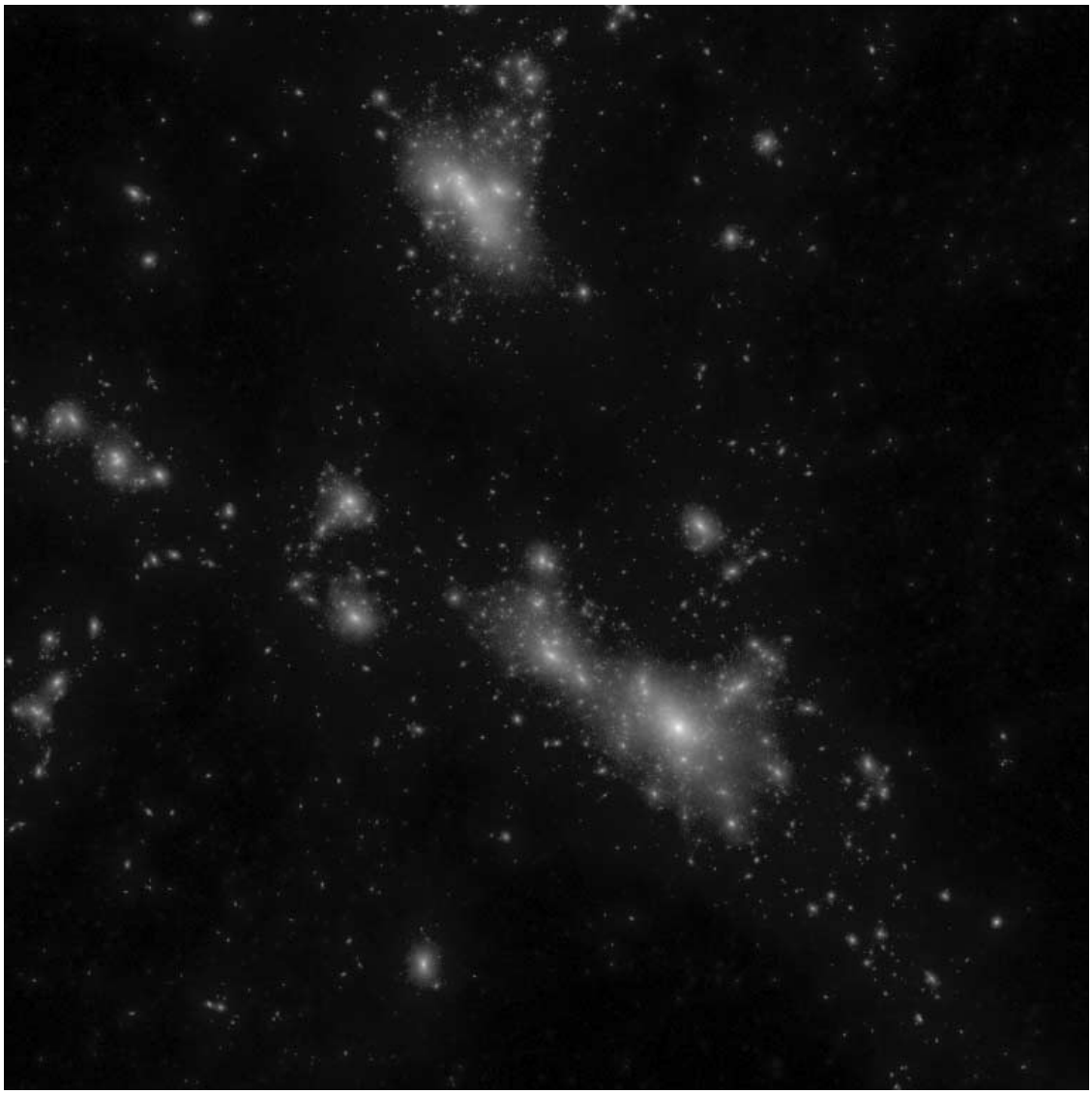

FIG. 1.—Snapshots from run S2 at $z = 0.58$. The length of the side is equal to 6.67 Mpc. [*See the electronic edition of the Journal for a color version of this figure*.]

At $r > 0.02$ Mpc or $r > 0.01r_v$, the density profiles are in good agreement with the profile given by equation (2) (the M99 profile) in all runs. This result is consistent with previous simulations performed with a few million particles (M99; Ghigna et al. 2000; Paper I; Paper II). The fitting here was done using M_v and the least-squares fit of $(\rho - \rho_{\rm M99})/\rho_{\rm M99}$ at $0.03 < r < 0.5$ Mpc. The scale radii r_0 obtained by the fitting are summarized in Table 2.

On the other hand, at $r < 0.01r_v$, we can see a shallowing of the cusp from the power -1.5 for all runs. The degree of the shallowing seems to increase as the radius decreases, which seemingly suggests that the inner cusp profile does not converge to a single slope. Moreover, the point where the profile starts to depart from the $r^{-1.5}$ cusp is different for different runs. For example, in run S1 the departure starts at $\sim 0.005r_v$, while at $\sim 0.02r_v$ in run L3. This means that *the density profile is not universal*.

In Figure 5 we plot the density profiles for all runs scaled by r_0 and ρ_0, together with the M99 profile. We can see that at $r/r_0 < 0.05$ all profiles are systematically shallower than the $r^{-1.5}$ cusp and that in this region run-to-run variation of the profile is significant. On the other hand, at $r/r_0 > 0.05$ the profiles are in good agreement with M99 profile. Although there are some dispersions from the M99 profile at $r/r_0 > 0.3$, they are not systematic.

In Figure 6 we plot the logarithmic slope of the density profile, $d\log(\rho)/d\log(r)$, as a function of radius, but for this figure, we averaged over a larger spherical shell whose width is $\log_{10}(\Delta r) = 0.137$. We can see a general trend that the shallowing inward becomes gradual at around $r \sim 0.2$ Mpc, which cannot be seen in less resolved simulations (e.g., Navarro et al. 2004)

3.3. *Reliability*

3.3.1. *Two-Body Relaxation*

We test the reliability of criterion (3) by using the simulations of the same initial condition as used in run S1 but with several different values for the total number of particles (N_v). Except for N, we used the same simulation parameters as in run S1. Figure 7 shows the cumulative mass $M_r(r)$ within the radiiof 0.1, 0.03, 0.01, 0.005, and 0.003 Mpc, as a function of

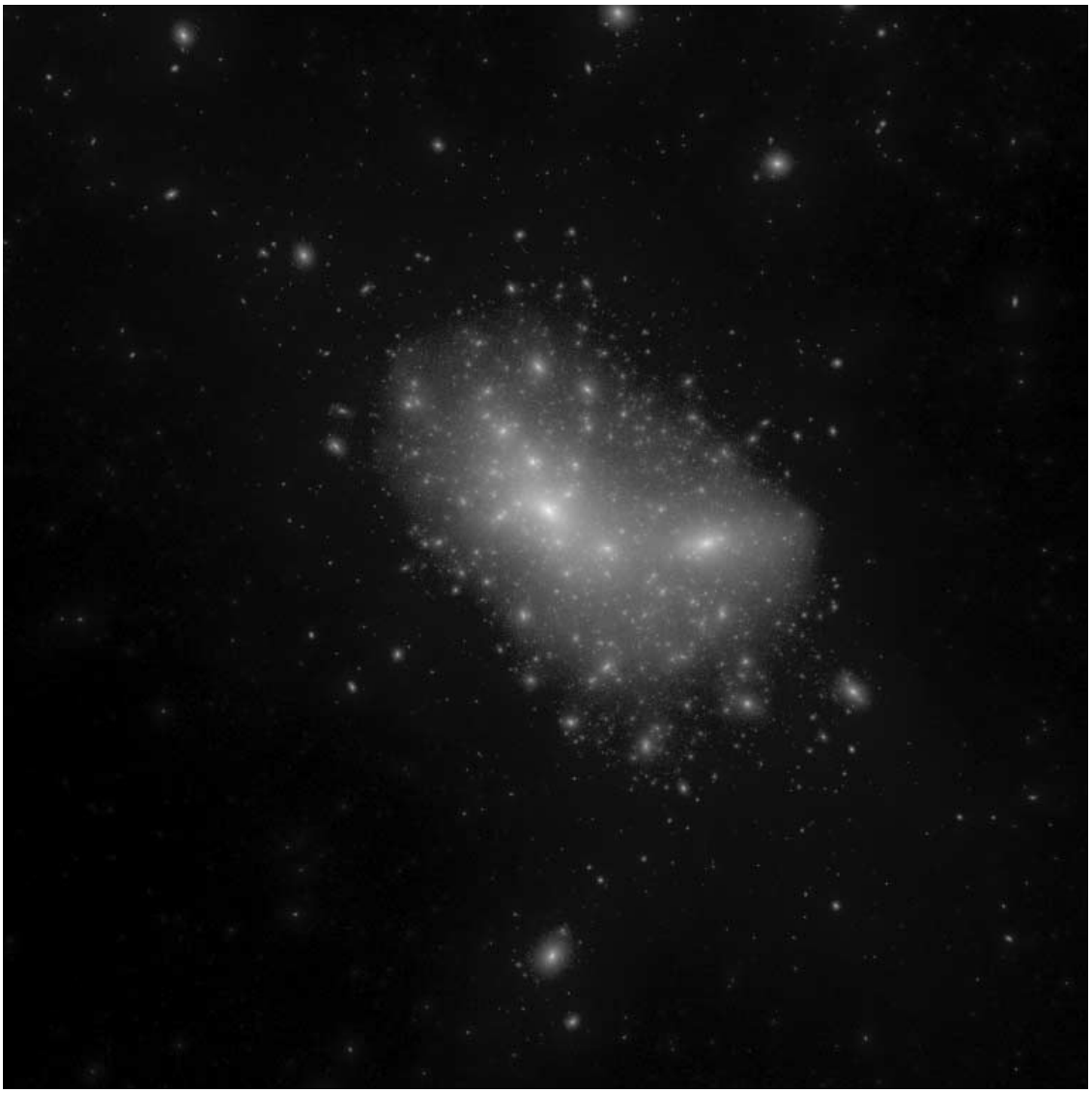

FIG. 2.—Same as Fig. 1, but at $z = 0$. [*See the electronic edition of the Journal for a color version of this figure.*]

time, for three simulations with 29 (run S1), 14, and 1 million particles within r_v. Figure 8 shows the final density profiles for three simulations. The vertical bars indicates the reliability limit obtained by criterion (3).

In Figure 7 we can see that the cumulative mass evolution obtained in the simulations with 29 and 14 millions particles are in good agreement for $r > 0.01$ Mpc. This agreement indicates that our criterion (0.009 Mpc for the 14 million particle run) gives a good reliability limit. In Figure 8 we can also see that the values of density ρ obtained in the simulations with 29 and 14 million particles are in good agreement outside the reliability limit of 14 million particle run (0.009 Mpc). The agreement of the averaged density is somewhat worse than that of the density. This is because the averaged density is an integrated quantity. Any error in the density inside the sphere of radius r affects the average density at radius r.

Recently, Power et al. (2003) proposed another reliability criterion for the two-body relaxation, given by

$$\frac{t_{\rm rel}(r)}{t} = \frac{N(r)}{8 \ln N(r)} \left(\frac{\rho_{\rm ave}}{200 \rho_{\rm crit}} \right)^{-1/2} > 0.6. \qquad (4)$$

Although their function form is different from ours and ignores the dependence on potential softening (see Fig. 3 of Paper I), it gives reliability limits similar to ours. For example, in run S1, the reliability limit given by their criterion is 0.007, 0.009, and 0.025 Mpc for simulations with 29, 14, and 1 million particles. These values are within 15% of our limit shown in Figure 8.

3.3.2. *Time Integration*

If the step size for the time integration is too large, it also influences the profile. We check whether the step size of time integration used in our simulations is small enough by performing simulations from the same initial model as run S1 but with several different step sizes (Δt). Except for Δt, we used the same simulation parameters as in run S1. Figure 9 show the cumulative mass within radii of 0.1, 0.03, 0.01, 0.005, and 0.003 Mpc, as a function of time, for three simulations with $\Delta t/(t_{\rm H} - t_i) = 1/4096$ (run S1), 1/2048, and 1/1024. Figure 10 show the profile of the density ρ for three simulations at $t/(t_{\rm H} - t_i) = 0.78125$. We plot the profile at this time since, in the simulation with $\Delta t/(t_{\rm H} - t_i) = 1/2048$, the merging process occurs near the center of halos at around $z = 0$.

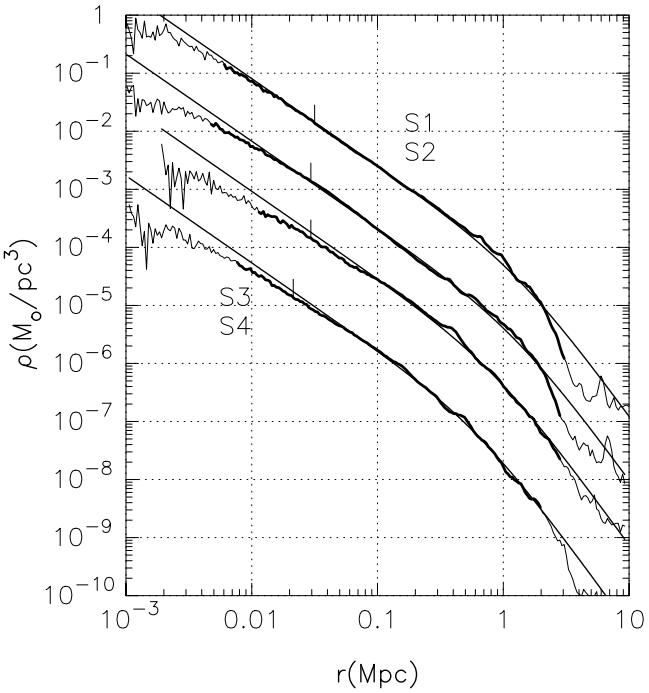

FIG. 3.—Density profile of the halos for all runs of the SCDM model at $z = 0$. Only the densities plotted by the thick lines satisfy criterion (3) in § 3.2 at $r < r_v$. The labels indicate the run name. The profiles except for run S1 are vertically shifted downward by 1, 2, and 3 dex for runs S2, S3, and S4, respectively. The vertical bars above the profiles indicate $0.01r_v$. The solid curves indicate the density profile given by eq. (2) (M99 profile). [*See the electronic edition of the Journal for a color version of this figure.*]

In these figures we can see that larger step size makes the central profile shallower. The density profile outside of 0.007 Mpc converges even by adapting 1/2048. Therefore, we can conclude that the step size of $\Delta t/(t_{\rm H} - t_i) = 1/4096$ did not introduce any numerical artifact.

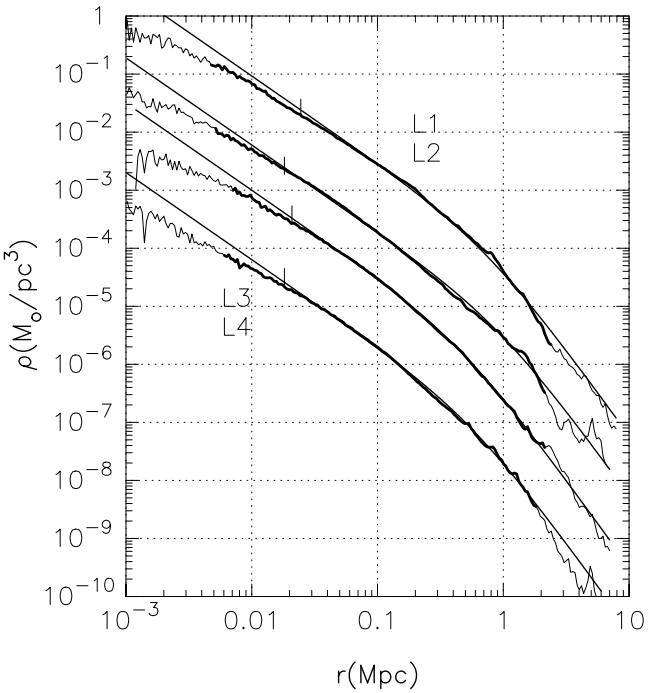

FIG. 4.—Same as Figure 3, but for the LCDM model. [*See the electronic edition of the Journal for a color version of this figure.*]

TABLE 2
FITTING PARAMETERS

RUN	r_0(Mpc)		r_c(Mpc)		r_v (Mpc)
	$\rho_{\rm M99}$	$\rho_{\rm NFW}$	$\rho_{\rm n1}$	$\rho_{\rm n2}$	
S1	1.36	0.41	0.70	0.0014	3.05
S2	1.31	0.40	0.68	0.0014	2.82
S3	0.88	0.42	0.60	0.0036	2.82
S4	0.66	0.29	0.44	0.0023	1.97
L1	0.75	0.31	0.50	0.0023	2.40
L2	0.95	0.33	0.52	0.0015	2.13
L3	0.48	0.23	0.34	0.0027	2.13
L4	0.57	0.26	0.38	0.0024	1.82

Power et al. (2003) investigated influences of the large step size on the profile and showed that the influence depends also on the softening length. They found that if potential softening length is larger than an optimal length, $\varepsilon \simeq 4r_v/\sqrt{N_v}$, a reliability limit is given by

$$\frac{t_c(r)}{t_c(r_v)} = 15\left(\frac{\Delta t}{t_0}\right)^{5/6}, \qquad (5)$$

and if softening length is smaller than the optical length more time steps are required than that given by criterion (5).

However, an application of the Power et al. (2003) criterion to our simulation results seems to give unphysically reliability limits. For example, in run S1, the reliability limit given by criterion (5) is 0.016, 0.038, and 0.083 Mpc for simulations with 1/4096, 1/2048, and 1/1024, respectively. From Figure 10, it is clear that these values are far too large. Such difference is possible, given the difference in the time integration methods used in Power et al. (2003) and ours. We used a constant time step in physical coordinates, while they used a variable step size in comoving coordinates.

3.3.3. *Potential Softening*

The potential softening also influences the profile. In order to see this effect, we simulated the same halo as run S1 but with a

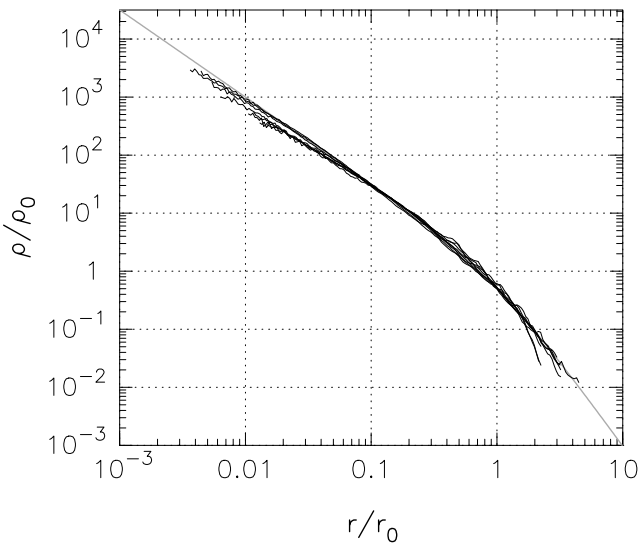

FIG. 5.—Density profiles for all runs scaled by r_0 and ρ_0 (Table 2). The solid curves indicate the density profile given by eq. (2) (M99 profile). [*See the electronic edition of the Journal for a color version of this figure.*]

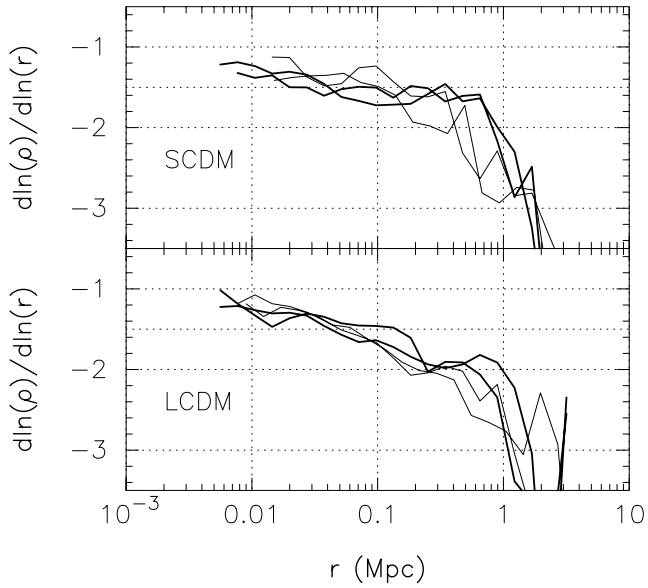

FIG. 6.—Logarithmic slope of the density profile, $d \log(\rho)/d \log(r)$, plotted as a function of radius. The thick curves indicate runs with higher resolution (runs S1, S2, L1, and L2).

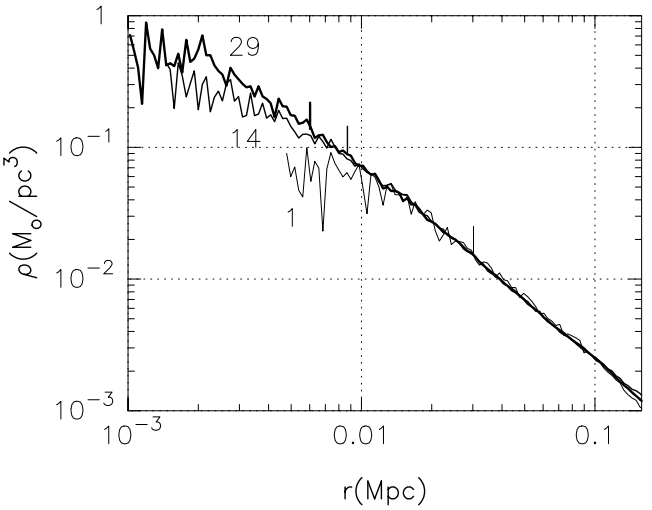

FIG. 8.—Density profiles for three simulations with 29 (run S1; *thick lines*), 14 (intermediate *lines*), and 1 (thin *lines*) million particles. The vertical bars indicate the reliability limits obtained by criterion (3) in § 3.2. [*See the electronic edition of the Journal for a color version of this figure.*]

smaller number of particles, $N = 5.5 \times 10^6$ and with different softening lengths (ε). In Figure 11 we plot the final density profile for models with $\varepsilon = 0.3$, 3, and 10 kpc. For these three models, the time step size is $\Delta t/(t_{\rm H} - t_i) = 1/2048$. In Figure 11 we can see that the central density is slightly lower for larger softening ($\varepsilon = 10$ kpc) inside around the softening length and is significantly lower for smaller softening ($\varepsilon = 0.3$ kpc).

For the 10 kpc run, the inner profile is affected by the force softening itself. Clearly, the density profile cannot be correct for a radius smaller than the softening size. However, we can also see that the maximum radius for which the softening has a visible effect is rather small. For $r > 2\varepsilon$, the effect is practically negligible. For the runs with 0.3 kpc softening, the reduction of the central density is primarily due to the error in the time integration, since the adoption of the smaller time step did increase the central density. These influences of potential softening were already discussed in Paper I (Fig. 9) and were comprehensively studied by Power et al. (2003).

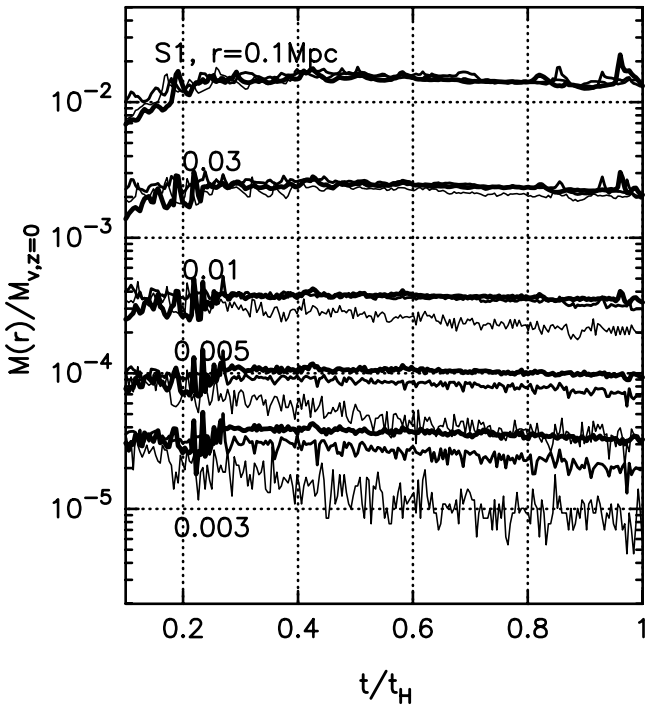

FIG. 7.—Cumulative mass within radii of 0.1, 0.03, 0.01, 0.005, and 0.003 Mpc, as a function of time, for three simulations with 29 (run S1; *thick lines*), 14 (intermediate *lines*), and 1 (thin *lines*) million particles. [*See the electronic edition of the Journal for a color version of this figure.*]

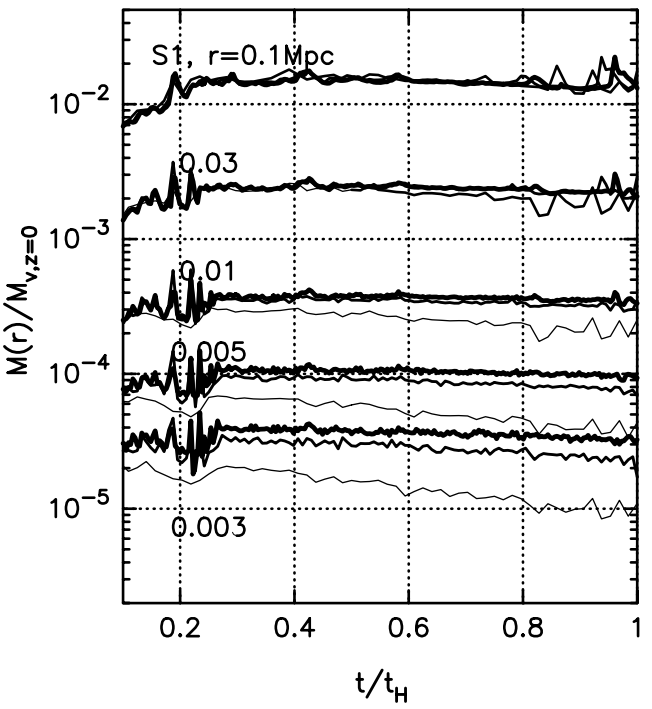

FIG. 9.—Same as Fig. 7, but for three simulations with $\Delta t/(t_{\rm H} - t_i) = 1/4096$ (run S1; *thick lines*), 1/2048 (*intermediate lines*), and 1/1024 (*thin lines*). [*See the electronic edition of the Journal for a color version of this figure.*]

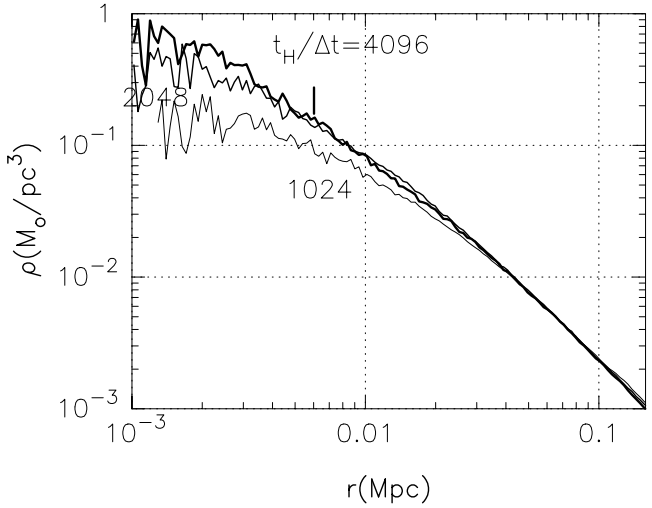

FIG. 10.—Density profiles for three simulations with $\Delta t/(t_H - t_i) = 1/4096$ (run S1; *thick lines*), 1/2048 (*intermediate*), and 1/1024 (*thin lines*). The vertical bars indicate the reliability limits obtained by criterion (3) in § 3.2. [*See the electronic edition of the Journal for a color version of this figure.*]

From the above tests, we conclude that the potential softening ($\varepsilon_{grav} = 1$ kpc for runs S1, S2, L1, and L2, 2 kpc for others) did not influence the density structure. The softening itself does not affect the density structure outside of the reliability limit obtained by the criterion for two-body relaxation, because the limit is more than 3 times larger than the softening length for all runs. The time integration is accurate enough for the density structure outside of the limit as shown in the previous section.

3.4. *Fitting by NFW Profile*

In Figure 12, we fit the density profiles for all runs to the NFW profile. The fitting here was done using M_v and the least-squares fit of $(\rho - \rho_{NFW})/\rho_{NFW}$ at $r < 0.5$ Mpc (down to the reliability limit). The scale radii r_0 obtained by the fitting are summarized in Table 2. We can see that the NFW profile is not

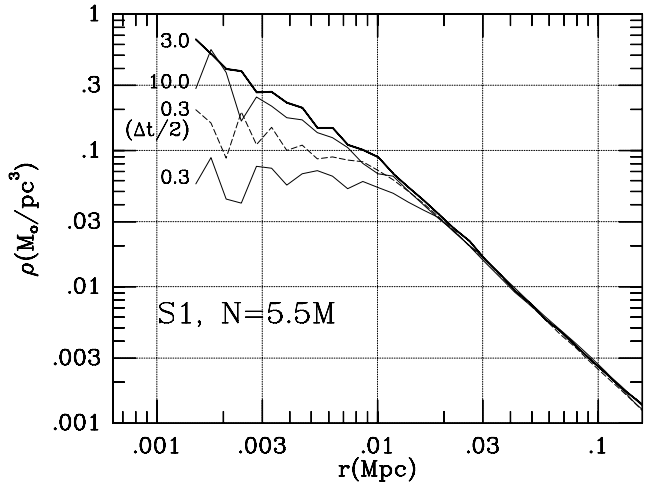

FIG. 11.—Density profiles for four simulations of the same model as run S1 with $N_v = 5.5 \times 10^6$ and $[\varepsilon, \Delta t/(t_H - t_i)] = (3.0$ kpc, $1/2048)$ (*thick lines*), (0.3 kpc; 1/2048) (*thin lines*), (10.0 kpc, 1/2048) (*thin lines*) and (0.3 kpc; 1/4096) (*dashed lines*). The numbers beside the profiles indicate the softening length in kiloparsecs.

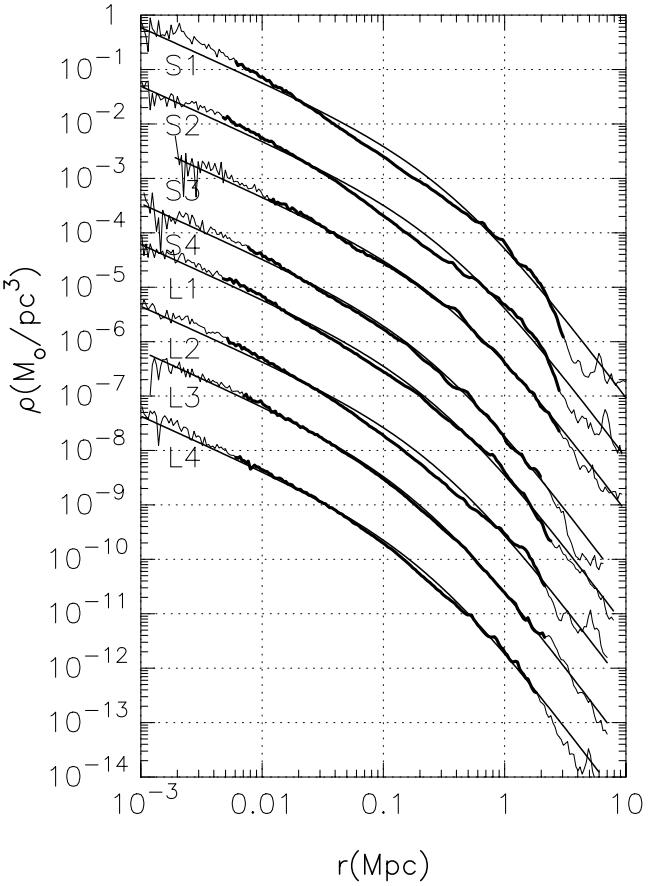

FIG. 12.—Density profiles for all runs. The solid curves indicate the density profile given by eq. (1) (NFW profile). [*See the electronic edition of the Journal for a color version of this figure.*]

in good agreement with simulation results, except for run L3. Figure 13 show the residual, $(\rho - \rho_{NFW})/\rho_{NFW}$, together with that for the M99 profile. The agreement with the NFW profile is not good in all radii, while that with the M99 profile is not good only in inner region ($r < 0.03$Mpc). Moreover, we can see that the sign of the residuals for NFW profile systematically change, which means the central slope of the NFW profile is too shallower.

3.5. *Evolution*

Figures 14 and 15 show the growth of the density profile for all runs. The virial radii and the masses within the virial radius at the redshift plotted are summarized in Table 3. We fit these profiles to the M99 profile. The fitting procedure is as same as that for Figure 3. The scale radii r_0 obtained by the fitting are summarized in Table 3.

At the inner region ($r < 0.03$ Mpc), we can see the density keeps almost unchanged from relatively higher redshift for all runs. This fact also can be seen in the evolution of the cumulative mass shown in Figure 7. This means that the density at the inner region is determined by that of the smaller halo that collapsed at higher redshift.

The density profile of the outer region is formed as the halo grows and shows universality. Moreover, the agreement with the M99 profile at higher redshift is very good down to the radius at which the cusp shallowing can be seen at $z = 0$, independent of the cosmological model that we simulated in this paper. Figure 16 shows the relation between the scale radius r_0 and density ρ_0 obtained by the fitting. We can see

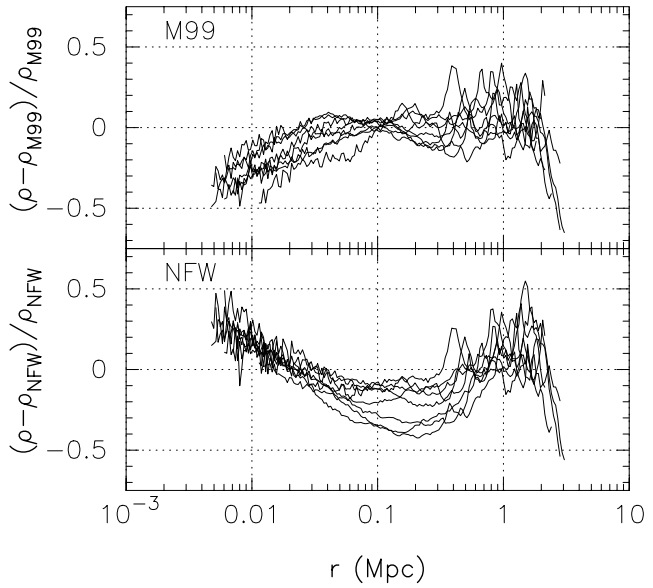

FIG. 13.—Residuals $(\rho - \rho_{M99})/\rho_{M99}$ and $(\rho - \rho_{NFW})/\rho_{NFW}$ as a function of radius.

clearly an evolutionary pass along a line, $\rho_0 \propto r_0^{-1.5}$, also independent of the cosmological model.

3.6. *Different Fitting*

In § 3.2 we see that the agreement with the M99 profile is not good at the inner region ($r < 0.02$ Mpc), and also that

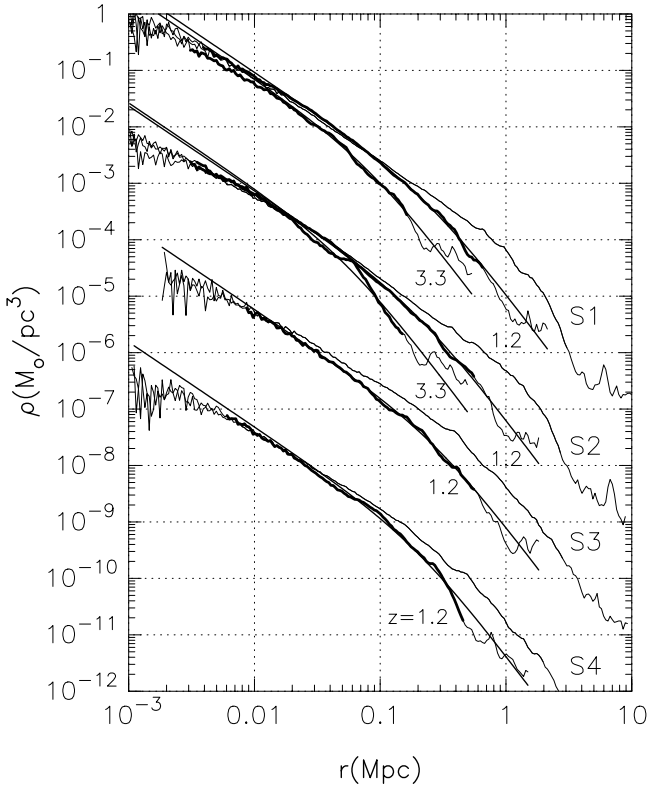

FIG. 14.—Evolution of density profile for all runs of the SCDM model. The numbers near profiles indicate the redshift. The profiles at $z = 0$ are plotted by the thin lines. Only the densities plotted in the thick lines satisfy criterion (3) in § 3.2 at $r < r_v$. The solid curves indicate the density profile given by equation (2) (M99 profile). [*See the electronic edition of the Journal for a color version of this figure*.]

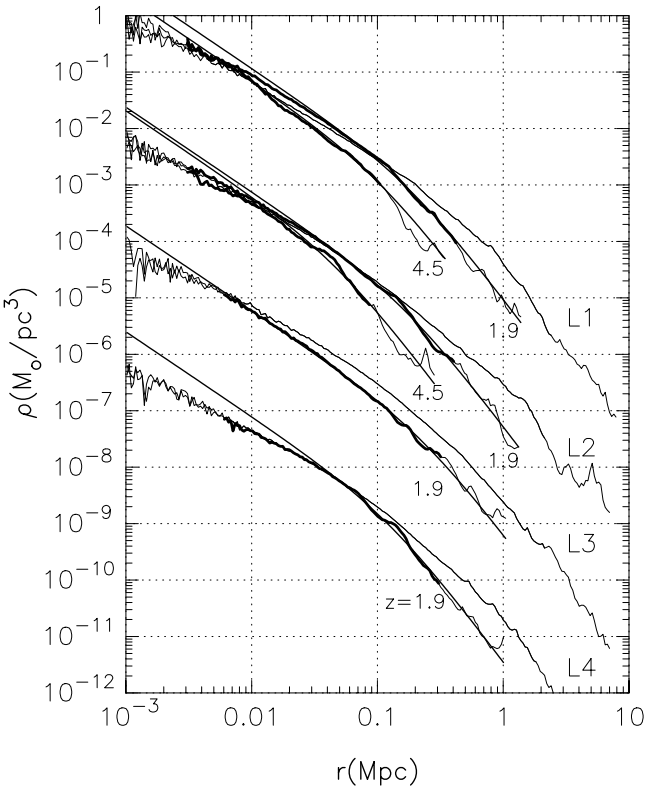

FIG. 15.—Same as Fig. 14, but for the LCDM model. [*See the electronic edition of the Journal for a color version of this figure*.]

with the NFW profile it is worse in the whole range of profiles in § 3.4. Therefore, it is worthwhile to fit the results to other profiles. Here we try to fit the results to two different profiles.

First, we fit the results to a profile that has an inner cusp shallower than that of the M99 profile and steeper than that of the NFW profile (fitting [1]), given as

$$\rho_{n1} = \frac{\rho_0}{(r/r_0)^{\alpha}\left[1 + (r/r_0)^{3-\alpha}\right]}, \tag{6}$$

where α is the power of the inner cusp and we set $\alpha = 1.3$. In Figure 17 we fit the density profiles to the profile given by equation (6). The fitting here was done using M_v and the

TABLE 3
PARAMETERS AT HIGHER REDSHIFT

Run	z	r_v (Mpc)	M_v ($M_\odot$)	r_0 (Mpc)
S1	3.3	0.16	1.9×10^{13}	0.085
	1.2	0.65	1.6×10^{14}	0.25
S2	3.3	0.15	1.6×10^{13}	0.056
	1.2	0.55	9.7×10^{13}	0.20
S3	1.2	0.55	9.8×10^{13}	0.29
S4	1.2	0.46	5.5×10^{13}	0.20
L1	4.5	0.11	1.4×10^{13}	0.11
	1.9	0.42	1.2×10^{14}	0.20
L2	4.5	0.086	7.3×10^{12}	0.05
	1.9	0.40	7.0×10^{13}	0.18
L3	1.9	0.32	5.4×10^{13}	0.24
L4	1.9	0.31	4.7×10^{13}	0.13

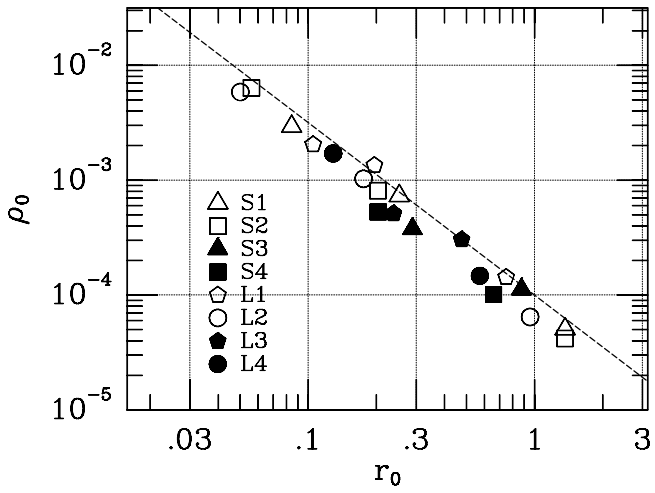

FIG. 16.—Scale density ρ_0 as a function of the scale radius r_0 (Table 3) at the redshift plotted in Figs. 14 and 15. The dashed line indicates $\rho_0 \propto r_0^{-1.5}$.

least-squares fit of $(\rho - \rho_{n1})/\rho_{n1}$ for $r < 0.5$ Mpc (down to the reliability limit). The scale radii r_0 obtained by the fitting are summarized in Table 2. Figure 18 shows the residual $(\rho - \rho_{n1})/\rho_{n1}$. The agreement is better than both the M99 and NFW profiles.

We also tried to add another power-law region ($\propto r^{\beta}$) to the M99 profile (fitting [2]), given as

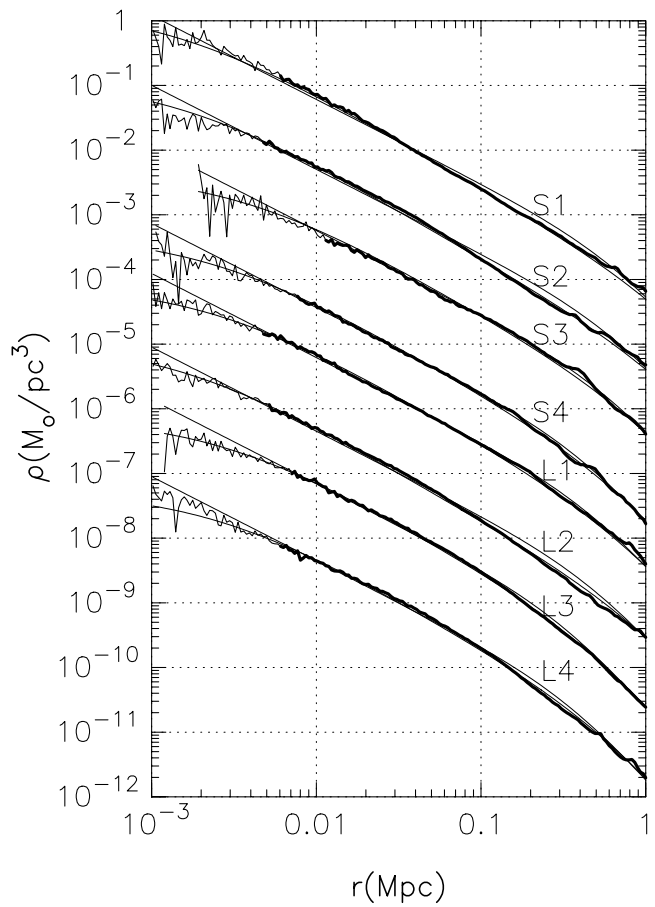

FIG. 17.—Density profiles for all runs at the inner region. The solid curves indicate the density profiles given by eqs. (6) and (7). [*See the electronic edition of the Journal for a color version of this figure.*]

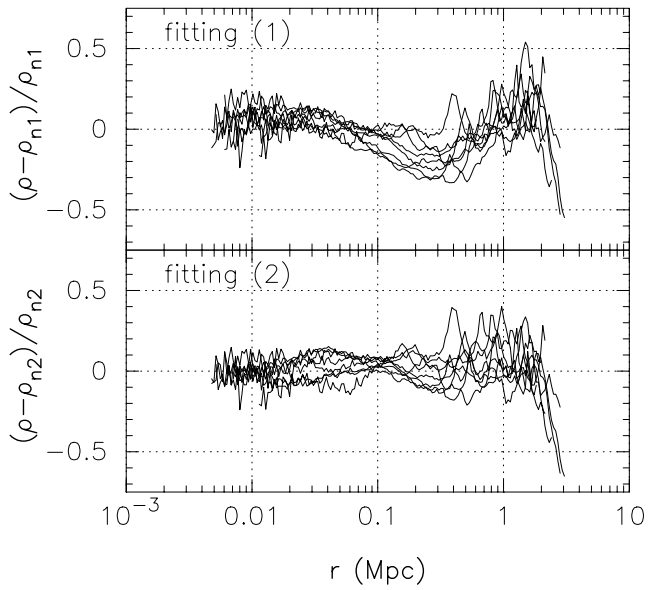

FIG. 18.—Residuals $(\rho - \rho_{n1})/\rho_{n1}$ and $(\rho - \rho_{n2})/\rho_{n2}$ as a function of radius

$$\rho_{n2} = \frac{\rho_0}{C_0(r/r_c)^{\beta}[1 + (r/r_c)]^{1.5-\beta}\left[1 + (r/r_0)^{1.5}\right]}, \quad (7)$$

where

$$1/C_0 = (r_0/r_c)^{\beta}[1 + r_0/r_c]^{1.5-\beta} \quad (8)$$

and r_c is another scale radius. Although this profile includes more parameters to fit, it is based on the observation that two different mechanisms might be working in the growth of the halo, as suggested by the analyses in § 3.5.

In Figure 17 we fit the density profiles to the profile given by equation (7). Here, for simplicity, we set $\beta = 0$ for all runs and, therefore, the equation (7) becomes

$$\rho_{n2} = \frac{\rho_0}{C_0[1 + (r/r_c)]^{1.5}\left[1 + (r/r_0)^{1.5}\right]}, \quad (9)$$

where

$$1/C_0 = [1 + (r_0/r_c)]^{1.5}. \quad (10)$$

The fitting here was done using r_0 obtained in the fitting to the M99 profile and the least-squares fit of $(\rho - \rho_{n2})/\rho_{n2}$ at $r < 0.5$ Mpc. The scale radii r_c obtained are summarized in Table 2. Figure 18 shows the residual, $(\rho - \rho_{n2})/\rho_{n2}$. As a matter of course, agreement is better than that for any other profile, since we increased the number of fitting parameters.

Unfortunately, in the present simulations, the region that we can use to determine which fitting formula is more appropriate is not so large. Further studies with simulations with higher resolution and a larger number of samples would be necessary.

4. CONCLUSION AND DISCUSSION

We performed *N*-body simulations of dark matter halo formation in SCDM and LCDM models. We simulated eight

halos whose mass range is 4.4×10^{14} to 1.6×10^{15} $M_\odot$ using up to 30 millions particles.

Our main conclusions are the following:

1. We found that, in all runs, the slope of inner cusp within $0.01r_v$ is shallower than -1.5, and the radius where the shallowing starts exhibits run-to-run variation, which means the profile is not universal.
2. We found that the profile is in agreement with the M99 profile for $r > 0.01r_v$ and is not in agreement with the NFW profile. We present different fitting formulae to describe the whole range of the simulation results.

Although we found interesting features in the inner structure of dark matter halo by new simulations with much higher resolution, we could not achieve a final understanding of the structure. One remaining question is whether or not the CDM halo has a flat core. Another question is whether the same shallowing can be seen in halos of galaxy or dwarf galaxy size. The origin of the inner structure is also still unclear. In order to answer these questions, we are now planning to perform larger simulations using a new GRAPE cluster system.

We are grateful to Yasushi Suto and Atsushi Taruya for many helpful discussions. We gratefully acknowledge the use of the initial condition generator in the publicly available code GRAPHIC2 developed by E. Bertschinger. We would like to thank all the people who have contributed to the development of the MDGRAPE-2 system at RIKEN. A part of the numerical computations were carried out on the GRAPE system at ADAC (the Astronomical Data Analysis Center) of the National Astronomical Observatory, Japan. This research was partially supported by Research for the Future Program (JSPS-RFTP 97P01102) and by the Grants-in-Aid (14740127 and 13440058) of the Japan Society for the Promotion of Science. Part of this work was carried out while A. K. was a special postdoctal researcher at RIKEN.

REFERENCES

Barnes, J. E. 1990, J. Comp. Phys., 87, 161
Barnes, J. E., & Hut, P. 1986, Nature, 824, 446
Bertschinger, E. 2001, ApJS, 137, 1
Eke, V. R., Cole, S., & Frenk C. S. 1996, MNRAS, 282, 263
Fukushige, T., & Makino, J. 1997, ApJ, 477, L9
———. 2001, ApJ, 557, 533 (Paper I)
———. 2003, ApJ, 588, 674 (Paper II)
Ghigna, S., Moore, B., Governato, F., Lake, G., Quinn, T., & Stadel, J. 2000, ApJ, 544, 616
Jing, Y. P., & Suto, Y. 2000, ApJ, 529, L69
———. 2002, ApJ, 574, 538
Kawai, A., Fukushige, T., Makino, J., & Taiji, M. 2000, PASJ, 52, 659
Kawai, A., Makino, J. 2003, in IAU Symp. 208, Astrophysical Supercomputing using Particle Simulations, ed. J Makino & P. Hut (San Francisco: ASP), 305
Kitayama, T., & Suto, Y. 1997, ApJ, 490, 557
Klypin, A., Kravtson, A. V, Bullock, J. S., & Primack, J. R. 2001, ApJ, 554, 903
Makino, J. 1991, PASJ, 43, 621
Moore, B., Governato, F., Quinn T., Statal, J., & Lake, G. 1998, ApJ, 499, L5
Moore, B., Quinn T., Governato, F., Statal, J., & Lake, G. 1999, MNRAS, 310, 1147
Navarro, J. F., Frenk, C. S., & White, S. D. M. 1996, ApJ, 462, 563
———. 1997, ApJ, 490, 493
Navarro, J. F., et al. 2004, MNRAS, in press
Power, C., Navarro, J. F., Jenkins, A., Frenk, C. S., White, S. D. M., Springel, V., Stadal, J., & Quinn, T. 2003, MNRAS, 338, 14
Spitzer, L. Jr. 1987, Dynamical Evolution of Globular Clusters (Princeton: Princeton University Press)
Susukita, R., et al. 2003, J. Comp. Phys., 155, 115
Warren, M. S., & Salmon, J. K., in Proc. of Supercompuing '93, 1993 (Los Alamos: IEEE Comp. Soc.), 12